

S3T-Former: A Purely Spike-Driven State-Space Topology Transformer for Skeleton Action Recognition

Naichuan Zheng
2022110134zhengnaichuan@bupt.edu.cn
School of Information and
Communication Engineering
Beijing University of Posts and
Telecommunications
Beijing, China

Hailun Xia*
xiahailun@bupt.edu.cn
School of Information and
Communication Engineering
Beijing University of Posts and
Telecommunications
Beijing, China

Zepeng Sun
szp2025140107@bupt.edu.cn
School of Information and
Communication Engineering
Beijing University of Posts and
Telecommunications
Beijing, China

Weiye Li
liweiyi@bupt.edu.cn
International School
Beijing University of Posts and
Telecommunications
Beijing, China

Yujia Wang
wangyujia@bupt.edu.cn
School of Economics and
Management
Beijing University of Posts and
Telecommunications
Beijing, China

Abstract

Skeleton-based action recognition is crucial for multimedia applications but heavily relies on power-hungry Artificial Neural Networks (ANNs), limiting their deployment on resource-constrained edge devices. Spiking Neural Networks (SNNs) provide an energy-efficient alternative; however, existing spiking models for skeleton data often compromise the intrinsic sparsity of SNNs by resorting to dense matrix aggregations, heavy multimodal fusion modules, or non-sparse frequency domain transformations. Furthermore, they severely suffer from the short-term amnesia of spiking neurons. In this paper, we propose the Spiking State-Space Topology Transformer (S3T-Former), which, to the best of our knowledge, is the first purely spike-driven Transformer architecture specifically designed for energy-efficient skeleton action recognition. Rather than relying on heavy fusion overhead, we formulate a Multi-Stream Anatomical Spiking Embedding (M-ASE) that acts as a generalized kinematic differential operator, elegantly transforming multimodal skeleton features into heterogeneous, highly sparse event streams. To achieve true topological and temporal sparsity, we introduce Lateral Spiking Topology Routing (LSTR) for on-demand conditional spike propagation, and a Spiking State-Space (S3) Engine to systematically capture long-range temporal dynamics without non-sparse spectral workarounds. Extensive experiments on multiple large-scale datasets demonstrate that S3T-Former achieves highly competitive accuracy while theoretically reducing energy consumption compared to classic ANNs, establishing a new state-of-the-art for energy-efficient neuromorphic action recognition.

CCS Concepts

• **Computing methodologies** → **Activity recognition and understanding.**

*Corresponding author.

Keywords

Skeleton-based Action Recognition, Spiking Neural Networks, Spiking Transformer, Kinematic Reasoning.

1 Introduction

Skeleton-based human action recognition has become a fundamental pillar in multimedia understanding, playing a pivotal role in applications ranging from embodied intelligent agents to immersive Extended Reality interactions[21]. Raw skeleton data naturally provides rich multimodal features (e.g., spatial joints and structural bones) that comprehensively depict human postures[8, 28]. In recent years, Artificial Neural Networks (ANNs), particularly Graph Convolutional Networks (GCNs)[1, 11] and Transformers[6, 26, 46], have achieved remarkable accuracy by fusing these multimodal skeletal features. However, extracting and aggregating multi-perspective information heavily relies on dense, floating-point multiply-accumulate (MAC) operations. When processing continuous, high-framerate action sequences, the exorbitant energy consumption of ANNs creates a severe bottleneck, prohibiting their deployment on resource-constrained, battery-powered edge devices that require "always-on" perception.

To address this energy crisis, Spiking Neural Networks (SNNs) have emerged as a promising neuromorphic paradigm, communicating via discrete binary spikes to replace power-hungry MACs with highly efficient accumulate (AC) operations[12, 14]. Recently, spiking-based Transformers have achieved remarkable success in various vision tasks[16, 33, 39, 40, 47]. In the specific realm of skeleton-based action recognition, pioneering efforts have introduced Spiking Graph Convolutional Networks (Spiking-GCNs) to model human dynamics[44, 45]. However, to process complex multimodal skeletal features, existing methods often resort to computationally heavy fusion modules or non-sparse frequency domain transformations. These workarounds inadvertently compromise the extreme spatial-temporal sparsity and the pure additive (AC) computational advantage that are the core tenets of SNNs. Furthermore,

in spatial topology modeling, they still inherit the dense matrix multiplication paradigm from traditional GCNs, failing to achieve conditional "on-demand" routing. Coupled with the intrinsic exponential decay ("short-term amnesia") of Leaky Integrate-and-Fire (LIF) neurons [15], it remains a formidable challenge for SNNs to capture long-range temporal causality and perform true sparse reasoning.

Driven by the critical need for a fully sparse architecture, we propose the Spiking State-Space Topology Transformer (S3T-Former). Inspired by retinal ganglion cells that fire sparsely in response to spatio-temporal gradients, we introduce the Multi-Stream Anatomical Spiking Embedding (M-ASE) as a generalized kinematic differential operator. Because Leaky Integrate-and-Fire (LIF) neurons are intrinsically designed to spike on dynamic changes, M-ASE systematically computes multi-order dynamics (identity, spatial, and temporal gradients) to translate dense skeletal features into rich, highly sparse event streams. This differential extraction explicitly maximizes the representational capacity of a single base modality, establishing an exceptionally powerful single-stream architecture for complex action reasoning.

Within the core transformer blocks, we completely redesign the attention mechanism to maintain this extreme sparsity. First, mimicking the functional division of Magnocellular and Parvocellular cells in the primate visual system [23, 24], we introduce Asymmetric Temporal-Gradient QKV (ATG-QKV). By forcing queries and keys to fire exclusively on dynamic motion gradients while preserving static structural features for values, ATG-QKV strictly silences background redundancies and pushes event-driven sparsity to the extreme. Subsequently, to overcome the dense topology bottleneck, we propose Lateral Spiking Topology Routing (LSTR). Instead of computing power-hungry GCN aggregations or $O(V^2)$ dense attention matrices, LSTR elegantly transforms spatial graph modeling into zero-MAC conditional additions. By propagating bound Key-Value spikes purely on-demand along the anatomical graph, LSTR accurately captures structural synergies while maintaining strictly discrete, event-driven spatial sparsity.

Finally, to cure the intrinsic "short-term amnesia" of LIF neurons without resorting to non-sparse spectral workarounds, we seamlessly integrate the Spiking State-Space (S3) Engine. By constructing a linear-complexity temporal memory pool, the engine systematically accumulates topological spike features over extended time windows. Coupled with a continuous U-Readout mechanism that directly utilizes the final membrane potential to preserve sub-threshold decision confidence, S3T-Former is empowered with robust long-range memory capacity. Together, these innovations enable the network to execute complex, long-sequence spatio-temporal reasoning under an ultra-low power envelope.

The main contributions of this work are summarized as follows:

- We propose **S3T-Former**, pioneering the first purely spike-driven Transformer architecture specifically designed for skeleton-based action recognition.
- We formulate **M-ASE** to translate multi-order biomechanical dynamics into rich event streams, maximizing the representational capacity of a single base modality without heavy intra-network fusion. Synergistically, we introduce **ATG-QKV** to force attention queries and keys to fire exclusively

on motion gradients, strictly silencing static redundancies and pushing event-driven sparsity to the extreme.

- We introduce **LSTR** to elegantly transform $O(V^2)$ dense spatial graph modeling into zero-MAC conditional additions, and the **S3-Engine** to construct a linear-complexity temporal memory pool that cures SNN short-term amnesia, achieving robust long-range reasoning under strict spatio-temporal sparsity.
- Extensive experiments on three large-scale datasets demonstrate that S3T-Former establishes a new state-of-the-art for SNNs and successfully outperforms several established ANNs in pure accuracy, while consuming only a tiny fraction of their theoretical energy.

2 Related Work

2.1 Skeleton-based Action Recognition

Skeleton-based action recognition fundamentally relies on modeling joint kinematics. While early methods utilized RNNs[7, 19, 20] and CNNs[42, 43], GCNs[2, 30, 35, 36] and Transformers[6, 26, 41, 46] now dominate by effectively capturing spatio-temporal dependencies and global contexts. To maximize performance, fusing multiple modalities (joints, bones, motions) is standard practice[3, 4, 17, 25]. However, these ANN paradigms rely heavily on power-hungry dense MAC operations, and complex multi-stream fusions further exacerbate computational burdens, prohibiting continuous efficient edge deployment.

2.2 Spiking Neural Networks

SNNs process information via discrete spikes, replacing power-hungry MACs with energy-efficient Accumulate (AC) operations [12, 14]. Recently, Spiking Transformers [16, 33, 39, 40, 47] have demonstrated immense potential in vision tasks by combining global receptive fields with high sparsity. For skeleton data, pioneering works [45] and [44] explored Spiking GCNs. However, to handle complex dynamics, they often resort to heavy fusion modules, non-sparse spectral transforms, and dense matrix aggregations. These workarounds inadvertently compromise the extreme spatio-temporal sparsity inherent to neuromorphic computing.

2.3 State-Space Models and Temporal Dynamics

Modeling long-range dependencies is critical for continuous action reasoning. State-Space Models (SSMs)[27, 31] efficiently capture ultra-long sequence contexts with linear complexity. In the neuromorphic domain, SNNs possess inherent temporal dynamics via the internal membrane potential of LIF neurons [9, 34]. However, their intrinsic exponential leakage causes severe "short-term amnesia" over long skeleton sequences [37]. Sustaining long-term semantic causality without reverting to dense temporal convolutions or non-sparse spectral filters remains a critical open challenge.

3 Method

In this section, we present S3T-Former, a purely spike-driven architecture designed for energy-efficient skeleton-based action recognition. Beyond circumventing the exorbitant energy consumption of ANNs, S3T-Former is specifically formulated to resolve three

critical bottlenecks in existing SNNs: multimodal representation collapse, pseudo-sparse graph topology, and short-term amnesia.

3.1 Preliminaries: Spiking Neuron Dynamics

Spiking Neural Networks process asynchronous event streams through the inherent temporal dynamics of spiking neurons. In this work, we adopt the widely-used Leaky Integrate-and-Fire (LIF) model as our foundational computing unit to ensure a purely event-driven architecture. The discrete-time dynamics of a LIF neuron at time step t are formulated as follows:

$$U[t] = \tau U[t-1] + I[t], \quad S[t] = \Theta(U[t] - U_{th}), \quad U[t] = U[t](1 - S[t]), \quad (1)$$

where $I[t]$ represents the presynaptic input current, $U[t]$ denotes the internal membrane potential, and $\tau \in (0, 1)$ is the membrane leakage factor controlling the exponential decay of historical states. When $U[t]$ exceeds the predefined firing threshold U_{th} , the Heaviside step function $\Theta(\cdot)$ triggers the emission of a binary spike $S[t] \in \{0, 1\}$. Following the spike emission, a hard reset mechanism immediately returns the membrane potential to the resting state. By relying exclusively on these binary spike communications, LIF neurons replace MAC operations with highly efficient, AC operations throughout the network.

3.2 Generalized Kinematic Differential Operator: M-ASE

Biological retinal ganglion cells encode visual information efficiently by firing sparsely in response to spatio-temporal gradients rather than absolute static intensities. Inspired by this neuromorphic mechanism, we propose the Multi-Stream Anatomical Spiking Embedding (M-ASE). Instead of functioning as a static linear projection, M-ASE is formulated as a generalized spatio-temporal kinematic differential operator. This design allows it to dynamically process any arbitrary base skeletal modality (e.g., joints, bones, or their temporal motions) and extract higher-order kinematic derivatives without heavy fusion architectures.

Given a generic base kinematic input $X \in \mathbb{R}^{T \times C_{in} \times N}$, where T , C_{in} , and N denote the temporal length, coordinate channels, and number of nodes, M-ASE systematically evaluates its multi-order dynamics. We formalize this by computing the zero-order identity state $X^{(0)}$, the first-order temporal gradient $X^{(T)}$, and the first-order spatial gradient $X^{(S)}$:

$$\begin{aligned} X^{(0)}[t] &= X[t], & X^{(T)}[t] &= X[t] - X[t-1], \\ X^{(S)}[t, :, v_{tgt}] &= X[t, :, v_{tgt}] - X[t, :, v_{src}], \end{aligned} \quad (2)$$

where $(v_{src}, v_{tgt}) \in \mathcal{E}_{anat}$ defines the anatomically connected pairs directing from the human center to the extremities. Note that $X^{(T)}[0]$ is initialized to zero.

This generalized formulation is highly scalable and physically interpretable. For instance, when X represents raw joint coordinates, $X^{(S)}$ and $X^{(T)}$ explicitly yield bone vectors and joint velocities. Crucially, when X represents bone vectors, $X^{(S)}$ intrinsically captures structural curvatures (joint angles), and $X^{(T)}$ yields angular velocities.

Subsequently, these three heterogeneous streams are independently projected into respective sub-embedding spaces via 1D convolutions and batch normalization, denoted as $\mathcal{F}_0(\cdot)$, $\mathcal{F}_S(\cdot)$, and

$\mathcal{F}_T(\cdot)$. Finally, the unified continuous representation is injected into a parametric LIF node to generate the initial highly sparse event stream $S_{in}[t] \in \{0, 1\}^{D \times N}$:

$$S_{in}[t] = \text{LIF} \left(\left[\mathcal{F}_0(X^{(0)}[t]) \parallel \mathcal{F}_S(X^{(S)}[t]) \parallel \mathcal{F}_T(X^{(T)}[t]) \right] \right), \quad (3)$$

where D is the total embedding dimension. By explicitly calculating these higher-order differential states, M-ASE ensures that the subsequent S3T-Former perceives structural deformations and transient kinetics exactly as biological vision does—focusing entirely on active changes, thereby pushing the input spike sparsity to the extreme.

3.3 Spiking State-Space Topology Block (S3T Block)

To capture long-range spatio-temporal dependencies at minimal energy costs, we design the S3T Block as the core building block of the network. Taking the highly sparse event stream S_{in} from the M-ASE module as its foundation, the S3T Block fundamentally decouples spatial aggregation and temporal integration. For a generic l -th block, let $S^{(l-1)} \in \{0, 1\}^{T \times D \times N}$ denote its input spike sequence (where $S^{(0)} = S_{in}$). We propose the (S3T) mechanism, which abandons traditional dense matrix multiplication. As illustrated in Fig. 1, the S3T module comprises three core innovations: ATG-QKV, LSTR, and the S3-Engine.

3.3.1 Asymmetric Temporal-Gradient QKV (ATG-QKV). In the primate visual system, Magnocellular (M) cells are highly sensitive to dynamic motion transients, while Parvocellular (P) cells specialize in encoding static structures [23]. Existing spiking attention mechanisms disregard this biological division, generating Query and Key spikes uniformly across all nodes, which inherently leads to severe computational redundancy. We introduce the ATG-QKV mechanism to force the intention queries (Q and K) to be dominated by physical motion gradients, while the content representation (V) relies on static structural features.

Given the input spike sequence $S^{(l-1)}$ to the l -th layer, we extract its absolute temporal gradient $S_{grad}[t] = |S^{(l-1)}[t] - S^{(l-1)}[t-1]|$. To prevent completely static nodes from suffering “feature starvation,” we introduce a Soft-ATG strategy that blends the gradient with the original state. **For notational simplicity, we omit the layer index (l) for all intermediate variables within the block:**

$$S_{dyn}[t] = \alpha S_{grad}[t] + (1 - \alpha) S^{(l-1)}[t], \quad (4)$$

where $\alpha \in \mathbb{R}^D$ is a learnable, channel-wise weighting parameter. Subsequently, these streams are independently projected into the attention space via distinct linear embedding functions, denoted as $\mathcal{F}_Q(\cdot)$, $\mathcal{F}_K(\cdot)$, and $\mathcal{F}_V(\cdot)$ (each comprising a 1D convolution followed by batch normalization). The query and key spikes are generated from the highly sparse dynamic stream S_{dyn} through parametric LIF neurons, whereas the value spikes are derived from the original stable stream $S^{(l-1)}$:

$$\begin{aligned} Q[t] &= \text{LIF}_Q(\mathcal{F}_Q(S_{dyn}[t])), & K[t] &= \text{LIF}_K(\mathcal{F}_K(S_{dyn}[t])) \\ V[t] &= \text{LIF}_V(\mathcal{F}_V(S^{(l-1)}[t])). \end{aligned} \quad (5)$$

For instance, during dynamic actions (e.g., running), rapidly moving limbs evoke intense motion gradients to trigger sparse Q and K spikes, while the relatively stationary torso provides stable V

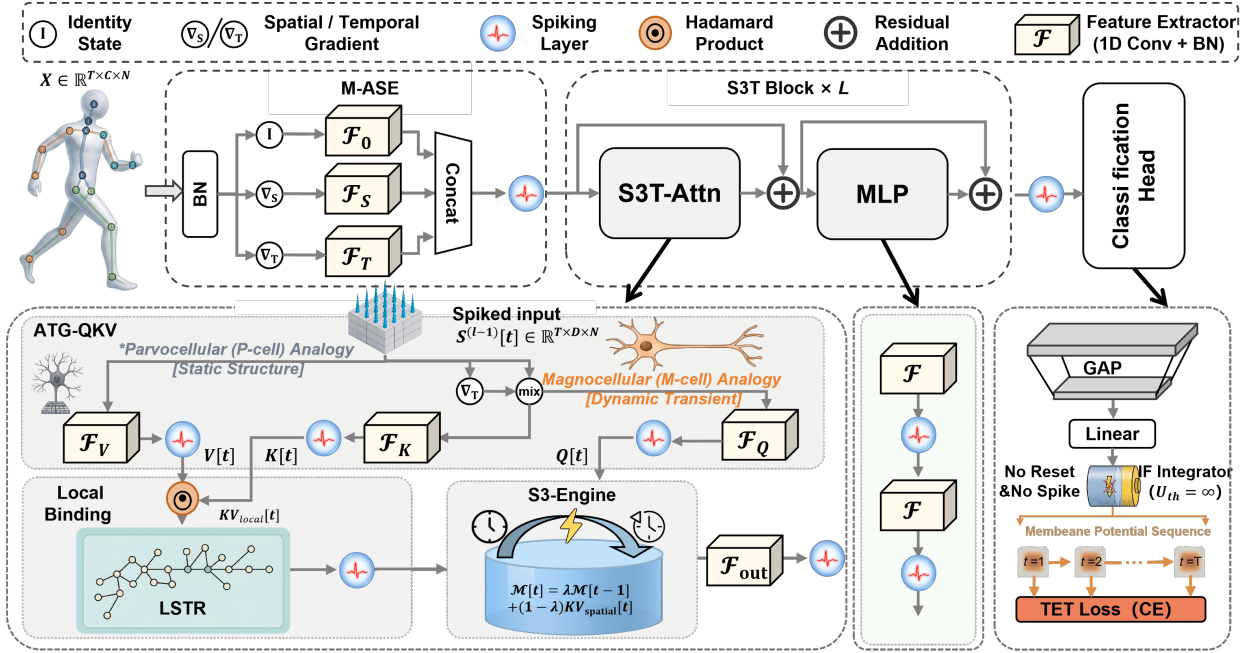


Figure 1: Overall architecture of the proposed Spiking State-Space Topology Transformer (S3T-Former). The input skeletal coordinates are first processed by the Multi-Stream Anatomical Spiking Embedding (M-ASE) to generate rich, multi-order (identity, spatial, and temporal) event streams. The core S3T Block employs a Spiking State-Space Topology Attention (S3T-Attn) module and a Spiking MLP. A non-spiking IF Integrator ($U_{th} = \infty$) serves as a lossless membrane potential readout, optimized directly with Temporal Efficient Training (TET) loss.

spikes to anchor the spatial structure. This biologically plausible asymmetry intrinsically reduces the average spike firing rate by one to two orders of magnitude compared to standard symmetric architectures.

3.3.2 Spiking State-Space Topology Attention. After obtaining the Q , K , and V spike streams, we abandon the $O(N^2 \times D)$ dense attention matrix computation. Instead, we perform an $O(N)$ spatio-temporal decoupled routing through three specialized steps:

Step A: Local Binding. We first bind the dynamic intention with the static content within each node via a pure spike Hadamard product:

$$KV_{local}[t] = K[t] \odot V[t] \quad (6)$$

Given the binary nature of spikes, this operation mathematically acts as a hard mask. Only nodes actively participating in motion are stamped and permitted to broadcast their features outward.

Step B: Lateral Spiking Topology Routing (LSTR). The masked KV_{local} spikes are subsequently propagated to neighboring joints along the natural human anatomical graph, as illustrated in Fig. 2. Formally, we model the human skeleton as a spatial graph $\mathcal{G} = (N, \mathcal{E})$, where N represents the N articular joints (nodes) and \mathcal{E} denotes the physical bones (edges). The base topology matrix $A_{base} \in \mathbb{R}^{N \times N}$ is strictly derived from the normalized adjacency matrix of \mathcal{G} , explicitly encoding the hard physical connectivities (e.g., the hand is connected to the elbow, but not directly to the foot).

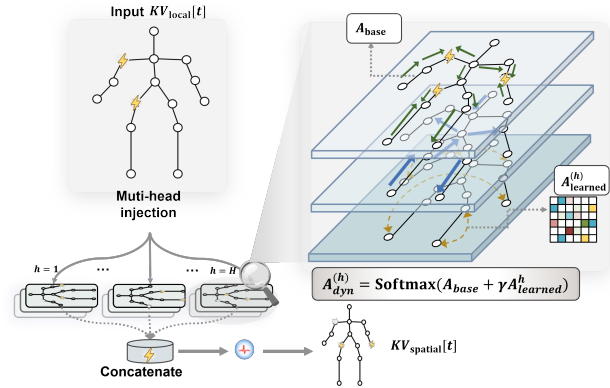


Figure 2: Lateral Spiking Topology Routing (LSTR). It decouples spatial anatomy into multi-head pathways, executing zero-MAC spatial feature broadcasts via conditional sparse additions.

To capture diverse structural dependencies with data-driven flexibility, we decouple the spatial routing into H independent attention heads. For each head $h \in \{1, \dots, H\}$, a head-specific dynamic topology matrix $A_{dyn}^{(h)}$ is defined:

$$A_{dyn}^{(h)} = \text{Softmax}(A_{base} + \gamma A_{learned}^{(h)}), \quad (7)$$

where A_{base} denotes the physical skeleton prior, $A_{learned}^{(h)}$ is a learnable parameter matrix initialized near zero to capture implicit, long-range synergistic dependencies, and γ is scaling factor. The spatial routing is performed as:

$$KV_{spatial}^{(h)}[t] = A_{dyn}^{(h)} \cdot KV_{local}^{(h)}[t]. \quad (8)$$

The routed features from all heads are concatenated and immediately re-spiked by a buffer LIF node to maintain the pure event-driven paradigm:

$$KV_{out}[t] = \text{LIF} \left(\left[KV_{spatial}^{(1)}[t] \parallel \dots \parallel KV_{spatial}^{(H)}[t] \right] \right). \quad (9)$$

Crucially, since A_{base} and $A_{learned}^{(h)}$ are input-independent, the Softmax normalization is computed only once per inference rather than at every time step. Consequently, the weighted aggregation of binary spikes $KV_{local}^{(h)}[t]$ mathematically degenerates into hardware-friendly, conditional sparse ACs strictly along the topological edges, circumventing dense MAC operations entirely. This design allows LSTR to achieve high-precision spatial modeling with nearly zero additional computational overhead.

Step C: Spiking State-Space (S3) Engine. To systematically cure the “short-term amnesia” of LIF neurons without reverting to dense temporal convolutions, we construct a non-recurrent state-space memory pool along the temporal axis, as illustrated in Fig. 3. The learnable decay factor is bounded via $\lambda = \text{Clamp}(\sigma(w_{decay}), 0.01, 0.99)$ to ensure stable long-term integration. The temporal memory state $\mathcal{M}[t]$ and the final attention output $O[t]$ are computed as:

$$\mathcal{M}[t] = \lambda \odot \mathcal{M}[t-1] + (1-\lambda) \odot KV_{spatial}[t], \quad (10)$$

$$O[t] = Q[t] \odot \mathcal{M}[t] \quad (11)$$

This architecture enables the current query spike $Q[t]$ to directly retrieve the memory pool $\mathcal{M}[t]$, which inherently encapsulates the global historical topology. It bounds the overall sequence complexity to linear $O(T)$, offering a true spatio-temporal receptive field. The attention output is linearly projected, aggregated via an output LIF node, and passed through a standard Spiking MLP block via residual connections to accomplish channel mixing. To facilitate strict reproducibility and intuitively demonstrate the purely discrete, zero-MAC nature of our attention mechanisms, the complete PyTorch-like pseudocode for the S3T Block is provided in Appendix C.

3.4 Overall Architecture and Membrane Readout

Unlike vanilla Vision Transformers that rely heavily on explicit positional encodings, S3T-Former inherently dispenses with them. Spatially, the LSTR mechanism naturally embeds relative topology by routing spikes strictly along anatomical edges. Temporally, the causal formulation of the S3-Engine, combined with M-ASE temporal gradients, intrinsically captures the unidirectional flow of time. This implicit spatio-temporal encoding eliminates redundant learnable parameters while strictly adhering to event-driven neuromorphic principles.

After the final block, we perform Global Average Pooling (GAP) over the spatial dimension N and aggregate the multi-person dimension to obtain a frame-level global representation $S_{global}^{(L)}[t] \in \mathbb{R}^D$. A

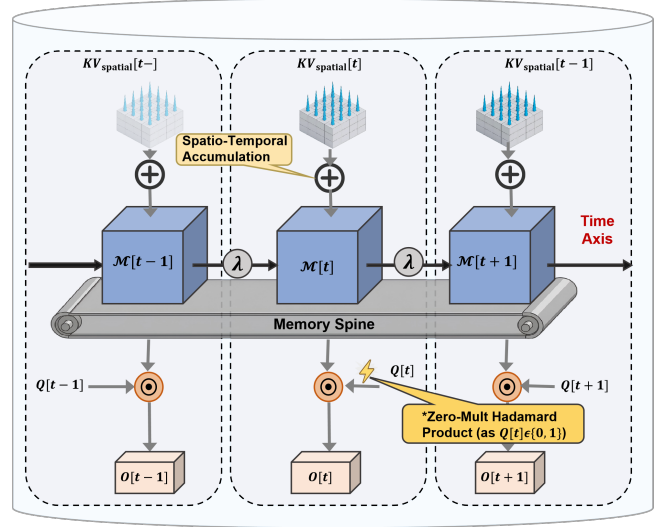


Figure 3: Spiking State-Space (S3) Engine. It constructs a linear-complexity temporal memory pool to integrate global spatio-temporal context without dense multiplications.

fully connected layer then maps this representation to a continuous classification current $I_c[t] \in \mathbb{R}^{C_{classes}}$ at each time step. To generate final predictions without the severe quantization errors of heuristic Integrate-and-Fire (IF) node ($U_{th} = \infty$) as a lossless temporal accumulator. The final classification distribution is directly decoded from the terminal membrane potential $U_{out}[T]$. Furthermore, this continuous frame-by-frame integration inherently enables Temporal Efficient Training (TET) [5], applying dense objective supervision at every time step to facilitate optimal convergence and mitigate gradient vanishing in deep SNNs.

4 Experiments

We comprehensively evaluate S3T-Former on three widely adopted skeleton-based action recognition benchmarks: NTU RGB+D 60 [29], NTU RGB+D 120 [18], and NW-UCLA [32]. Due to space constraints, detailed dataset protocols and implementation configurations are deferred to Appendices A and B. In this section, we first benchmark our model against state-of-the-art ANNs and SNNs to demonstrate its superior accuracy-efficiency trade-off. Subsequently, we provide extensive ablation studies and qualitative visualizations to dissect the individual contributions, routing interpretability, and extreme spiking sparsity of our core architectural designs.

4.1 Comparison with State-of-the-Art Architectures

We benchmark S3T-Former against state-of-the-art architectures, spanning advanced Artificial Neural Networks (ANNs) and Spiking Neural Networks (SNNs).

Table 1: Comparison with prior ANN- and SNN-based models on NTU RGB+D, NTU RGB+D 120, and NW-UCLA datasets. ‘Mod.’ denotes input modalities (J: Joint, B: Bone, JM: Joint Motion, BM: Bone Motion). The network type and architecture paradigm are denoted in brackets (e.g., [ANN-GCN], [SNN-Trans.]).

Model		Mod.	T	Param. (M)	FLOPs (G)	NTU RGB+D Xs(%) Xv(%)		NTU RGB+D 120 Xs(%) Xt(%)		NW-UCLA (%)
Part-aware LSTM [7]	[ANN-RNN]	J	-	-	-	62.9	70.3	25.5	26.3	-
ST-GCN [36]	[ANN-GCN]	J	-	3.10	3.48	81.5	88.3	70.7	73.2	-
2S-AGCN [30]	[ANN-GCN]	J+B	-	3.48	37.32	88.5	95.1	82.5	84.3	-
Shift-GCN [3]	[ANN-GCN]	All	-	-	10.00	90.7	96.5	85.3	86.6	94.6
MS-G3D [22]	[ANN-GCN]	J+B	-	3.19	48.88	91.5	96.2	86.9	88.4	-
CTR-GCN [2]	[ANN-GCN]	All	-	1.46	7.88	92.4	96.8	88.9	90.6	96.5
Hyperformer [46]	[ANN-Trans.]	J	-	2.60	14.80	90.7	95.1	86.6	88.0	-
Hyperformer (4 ensemble) [46]	[ANN-Trans.]	All	-	2.60	59.20	92.9	96.5	89.9	91.3	96.7
SkateFormer [6]	[ANN-Trans.]	J	-	2.03	3.62	92.6	97.0	87.7	89.3	-
SkateFormer (4 ensemble) [6]	[ANN-Trans.]	All	-	2.03	14.48	93.5	97.8	89.8	91.4	98.3
Spikformer [47]	[SNN-Trans.]	J	4	4.78	24.07	73.9	80.1	61.7	63.7	85.4
Spike-driven Transformer [39]	[SNN-Trans.]	J	4	4.77	23.50	73.4	80.6	62.3	64.1	83.4
Spike-driven Transformer V2 [38]	[SNN-Trans.]	J	4	11.47	38.28	77.4	83.6	64.3	65.9	89.4
Spiking Wavelet Transformer [10]	[SNN-Trans.]	J	4	3.24	19.30	74.7	81.2	63.5	64.7	86.7
STAtten [16]	[SNN-Trans.]	J	4	3.19	18.78	72.8	79.7	60.3	61.7	82.8
MK-SGN [45]	[SNN-GCN]	All	4	2.17	7.84	78.5	85.6	67.8	69.5	92.3
Signal-SGN [44]	[SNN-GCN]	J	16	1.74	1.62	80.5	87.7	69.2	72.1	92.7
Signal-SGN [44]	[SNN-GCN]	J+B	16	1.74	3.24	82.5	89.2	71.3	74.2	93.1
Signal-SGN (4 ensemble) [44]	[SNN-GCN]	All	16	1.74	6.48	86.1	93.1	75.3	77.9	95.9
S3T-Former (D=256)	[SNN-Trans.]	J	8	4.80	0.957	82.83	89.65	74.01	78.98	93.1
S3T-Former (D=256)	[SNN-Trans.]	J	16	4.80	1.914	83.61	90.42	74.78	79.45	93.8
S3T-Former (D=256)	[SNN-Trans.]	J	32	4.80	3.829	84.50	91.15	75.58	80.01	94.3
S3T-Former (D=384)	[SNN-Trans.]	J	16	10.73	4.287	84.94	91.20	75.76	80.24	94.8
S3T-Former (D=384)	[SNN-Trans.]	J	32	10.73	8.574	85.12	91.5	76.12	80.65	95.1
S3T-Former (D=384)	[SNN-Trans.]	J+B	16	10.73	8.574	86.30	93.15	79.36	82.15	95.8
S3T-Former (D=384, Ensemble)	[SNN-Trans.]	All	16	10.73	17.14	87.35	94.05	81.68	84.12	96.6

Param. represents the model size. FLOPs represent theoretical floating-point operations. For SNN methods, the T column explicitly denotes the neuromorphic simulation time window. We omit T for ANN models to avoid conceptual confusion with their raw input frame length. "All" refers to the fusion of J, B, JM, and BM modalities. **Evaluation protocols are denoted as Xs (Cross-Subject), Xv (Cross-View), and Xt (Cross-Setup).**

Crucially, compared to the current neuromorphic state-of-the-art, Signal-SGN [44], our S3T-Former demonstrates absolute superiority. Under the exact same simulation window ($T = 16$) and single joint (J) modality, our base model ($D = 256$) achieves 83.61% on NTU RGB+D 60 (X-Sub), outperforming Signal-SGN (80.5%) by a significant +3.11% margin. Scaling the embedding dimension ($D = 384$) further widens this gap to +4.44% (84.94%). This dominance is even more pronounced on the highly challenging NTU RGB+D 120 dataset, where our ensemble model achieves 81.68% (X-Sub), completely eclipsing the Signal-SGN ensemble (75.3%) by an astounding +6.38%. This compelling evidence proves that our purely spike-driven topology attention and state-space memory systematically capture complex, long-range temporal dynamics far better than existing Spiking GCNs. Furthermore, S3T-Former shatters the performance ceiling of early Spiking Transformers (e.g., Spikformer, Spike-driven Transformer V2), which plateaued around 73%-77% on NTU-60 due to their reliance on unoptimized dense attention and pseudo-temporal modeling.

When compared against traditional ANNs, S3T-Former showcases an unparalleled accuracy-efficiency trade-off. While recent ANN models (e.g., Hyperformer, SkateFormer) achieve impressive peak accuracy, they inherently suffer from exorbitant computational burdens driven by power-hungry floating-point MAC operations. For instance, SkateFormer’s ensemble requires 14.48G FLOPs, and Hyperformer demands up to 59.20G. In stark contrast, our single-stream S3T-Former ($D = 256$) requires merely 1.91G theoretical FLOPs. More importantly, a direct FLOP-to-FLOP comparison severely underestimates our neuromorphic advantage. As detailed in Appendix D, S3T-Former executes the vast majority of its operations as binary, sparse Synaptic Operations (SOPs). By replacing dense MACs with AC operations and perfectly silencing static spatial nodes via the ATG-QKV mechanism, conservative estimations guarantee that our model consumes less than 10% of the physical energy required by standard ANN counterparts. Despite this extreme power reduction, S3T-Former achieves the rare neuromorphic feat of surpassing several established ANN models

Table 2: Progressive core build-up ablation study of S3T-Former. UR: U-Readout, S3: S3-Engine, LS: LSTR, MA: M-ASE, AQ: ATG-QKV. FLOPs are reported for a single person.

Step	Components					Param. (M)	FLOPs (G)	Acc (%)
	UR	S3	LS	MA	AQ			
1 (Baseline)						4.77	1.91	76.32
2	✓					4.77	1.91	77.15
3	✓	✓				4.77	1.91	78.68
4	✓	✓	✓			4.78	1.91	80.24
5	✓	✓	✓	✓		4.78	1.91	82.77
6	✓	✓	✓	✓	✓	4.78	1.91	83.80

in pure accuracy (e.g., our 84.94% explicitly beats ST-GCN’s 81.5% on NTU-60 X-Sub), establishing a definitive new state-of-the-art for energy-efficient action recognition.

4.2 Ablation Studies

To deeply analyze the underlying mechanisms of S3T-Former and validate the efficacy of our architectural designs, we conduct extensive ablation studies on the NTU RGB+D 60 (Cross-Subject) dataset. Our evaluation spans from macroscopic to microscopic dimensions: first, we progressively integrate our core modules to validate their synergistic effects and overall performance gains (Sec.4.2.1); second, we explore the lateral topology routing of the LSTR module to verify the necessity of fusing physical priors with data-driven routing (Sec.4.2.2); Finally, we dissect the temporal state-space memory and continuous readout strategies of the S3-Engine (Sec.4.2.3).

4.2.1 Progressive Core Build-up. We evaluate the individual and synergistic contributions of our proposed modules by progressively integrating them into a "Vanilla Spiking Transformer" baseline. This baseline is constructed following the standard Spikformer architecture, utilizing LIF neurons and dense attention on a single joint stream. Notably, to ensure a rigorous "apples-to-apples" ablation, we equip this baseline with our optimized training recipe (e.g., an extended simulation window of $T = 16$ and Temporal Efficient Training). Consequently, it establishes a solid foundation of 76.32% Top-1 accuracy—significantly outperforming the skeleton-adapted Spikformer baseline (73.9%, $T = 4$) reproduced in prior works [45]. As shown in Table 2, building upon this strong baseline, the integration of U-Readout (Step 2) and the S3-Engine (Step 3) enhances performance to 78.68% (+2.36%), demonstrating the critical role of continuous membrane potential dynamics and temporal state-space trajectories in mitigating the "short-term amnesia" inherent in traditional SNNs. The addition of LSTR (Step 4) further boosts accuracy to 80.24% by enforcing anatomically-guided sparse routing. A significant leap to 82.77% occurs with M-ASE (Step 5), proving that multi-order kinematic representations—joints, bones, and motion—fully unlock the potential of topological routing. Finally, our full S3T-Former (Step 6) achieves a peak accuracy of 83.80% via the ATG-QKV mechanism, which optimizes attention logic through asymmetric temporal gradients. Remarkably, this substantial +7.48% overall improvement is achieved with a practically

imperceptible computational footprint (adding merely 0.01M parameters with mathematically negligible FLOPs overhead), showcasing a successful decoupling of accuracy enhancement from computational inflation.

Table 3: Comprehensive ablation of LSTR routing strategies, multi-head configurations (H), and scaling factors (γ).

Routing Strategy	Heads	Factor	Acc
	H	γ	(%)
Dense (No Prior)	-	-	78.68
Physical Only (Static)	-	-	79.12
LSTR (Hybrid)	Shared ($H = 1$)	0.5	81.45
LSTR (Hybrid)	Split ($H = 4$)	0.1	81.75
LSTR (Hybrid)	Split ($H = 4$)	1.0	81.20
LSTR (Hybrid)	Split ($H = 4$)	0.5	82.91
LSTR (Hybrid)	Split ($H = 8$)	0.1	82.34
LSTR (Hybrid)	Split ($H = 8$)	1.0	81.92
LSTR (Hybrid)	Split ($H = 8$)	0.5	83.80

4.2.2 Exploration of LSTR. We evaluate the LSTR module against Dense (all-to-all) and Static Physical baselines (Table 3), demonstrating that our hybrid approach effectively balances structural constraints with global context to filter redundant spatial noise. We further ablate the multi-head configurations (H) and the scaling factor (γ). Progressively increasing H to 8 yields consistent gains, proving that independent heads effectively specialize in distinct kinematic sub-structures to enhance representational diversity. Simultaneously, a moderate scaling factor of $\gamma = 0.5$ emerges as the optimal sweet spot: a smaller value (0.1) overly restricts routing to rigid skeletal links, while a larger value (1.0) diminishes the stabilizing physical prior and amplifies spatial noise. Ultimately, configuring LSTR with $H = 8$ and $\gamma = 0.5$ perfectly grounds the network in physical reality while maintaining vital data-driven adaptability.

Table 4: Ablation of S3-Engine and output readout strategies.

Temporal Memory	Decay Factor λ	Readout Type	Acc (%)
None	-	Spike-rate	76.32
None	-	U-Readout	77.15
S3-Engine	Learnable	Spike-rate	78.68
S3-Engine	Fixed (0.5)	U-Readout	79.42
S3-Engine	Linear	U-Readout	81.18
S3-Engine	Learnable	U-Readout	83.80

4.2.3 Synergy of S3-Engine and U-Readout. We investigate the synergy between the supplemental S3-Engine and the U-Readout decoding strategy. As shown in Table 4, the baseline without the S3-Engine yields 76.32% under standard Spike-rate decoding, and upgrading solely to U-Readout provides only a marginal gain (77.15%).

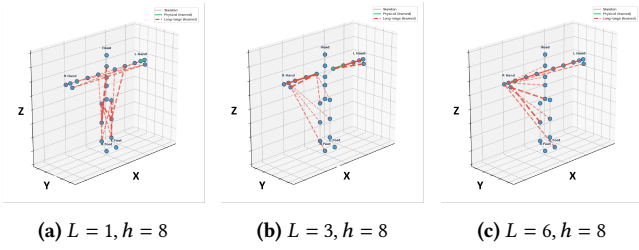


Figure 4: Visualization of the dynamic topology matrix $A_{dyn}^{(h)}$ (Eq. 7) across different network depths for head $h = 8$.

Furthermore, even when introducing a fully learnable S3-Engine to preserve historical trajectories, performance remains bottlenecked at 78.68% if forced through a discrete Spike-rate classifier, as the rich continuous temporal context is severely degraded by non-differentiable quantization errors. The network’s true potential is unlocked only when these mechanisms are synergistically combined: by employing U-Readout to directly utilize the final accumulated membrane potential $U_{out}[T]$, the model completely bypasses quantization loss to fully exploit the sophisticated temporal states, achieving a peak accuracy of 83.80%. This demonstrates a strict co-dependency where the S3-Engine safeguards long-range temporal causality, and U-Readout ensures absolute information fidelity during final decision decoding.

4.3 Qualitative Results

4.3.1 Visualization of Topological Routing. To illustrate how independent heads specialize in distinct sub-structures, we visualize the dynamic topology $A_{dyn}^{(8)}$ for a representative head ($h = 8$, Fig. 4). It reveals a profound layer-wise convergence: shallow layers ($L = 1$) aggressively explore global contexts, while deeper layers ($L = 6$) actively prune irrelevant links. Ultimately, the topology sharpens into a focused semantic cluster (coordinating the dominant arm and torso), demonstrating LSTR’s ability to filter spatial noise and distill essential kinematic signatures.

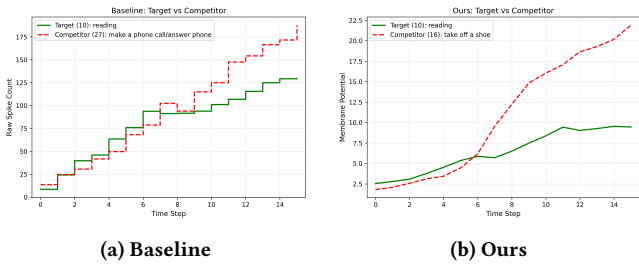


Figure 5: Target vs. Competitor dynamics. U-Readout avoids the staircase effect of Spike Counting.

4.3.2 Output Dynamics Analysis. As shown in Fig. 5 and 6, the baseline spike-counting exhibits a discrete "staircase effect," suffering from severe sub-threshold quantization loss. Conversely, U-Readout generates smooth confidence trajectories from membrane potentials, preserving fine-grained temporal evolution. This

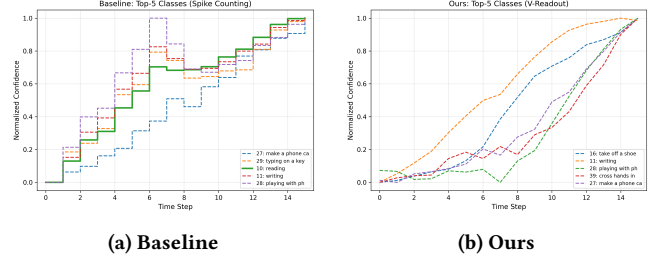


Figure 6: Top-5 class progression. U-Readout provides smoother, more distinguishable trajectories.

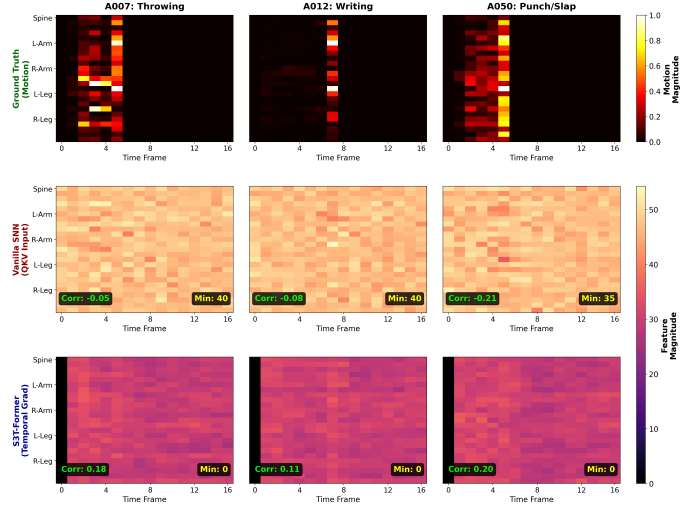


Figure 7: Visualization of spatio-temporal activation maps across three distinct action classes.

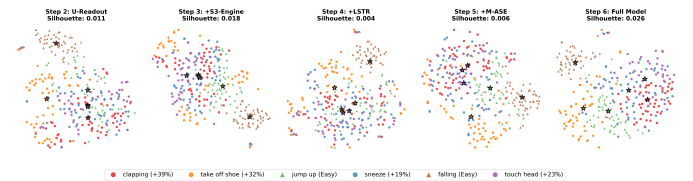


Figure 8: t-SNE visualization of learned feature distributions for visually confusing action classes.

establishes a distinctly clearer margin between the target class and its strongest competitor, overcoming the resolution limitations of traditional SNN decoding.

4.3.3 Spatio-Temporal Sparsity Analysis. Unlike vanilla SNNs that maintain energy-wasting background noise for static joints (yielding negative motion correlations, e.g., -0.21), S3T-Former completely silences static frames (Fig. 7). Activations peak exclusively during meaningful joint displacements, yielding consistent positive correlations across diverse actions. This confirms ATG-QKV successfully eradicates spatial redundancy, dynamically allocating computations strictly to salient kinetic events.

4.3.4 *Feature Representation Discriminability.* We visualize feature distributions using t-SNE (Fig. 8) for four visually confusing classes with similar localized movements. S3T-Former successfully maps these challenging actions into well-separated clusters with tight intra-class variance. Remarkably, even highly ambiguous actions like "Reading" and "Writing"—sharing almost identical minimal facial-proximal dynamics—are clearly disentangled, confirming robust semantic decision boundaries. Due to space constraints, the full confusion matrix and layer-wise semantic sparsity funnels are deferred to Appendix E.

5 Conclusion

In this paper, we propose S3T-Former, the first purely spike-driven Transformer architecture specifically designed for energy-efficient skeleton action recognition. To overcome multimodal fusion overhead, we introduce the Multi-Stream Anatomical Spiking Embedding (M-ASE) to enrich the base representation by translating multi-order kinematics into rich event streams. Synergistically, the Asymmetric Temporal-Gradient QKV (ATG-QKV) mechanism enforces extreme computational sparsity by silencing static background and firing exclusively on dynamic motion. Furthermore, we elegantly resolve the dense topological and temporal bottlenecks of traditional SNNs through Lateral Spiking Topology Routing (LSTR) for zero-MAC spatial propagation, and the Spiking State-Space (S3) Engine for robust, long-range causal memory. Extensive experiments demonstrate that S3T-Former establishes a definitive new neuro-morphic state-of-the-art—outperforming existing Spiking GCNs by up to +6.38%—while consuming less than 10% of the energy of comparable ANNs. Future work will explore adaptive localized firing to resolve the inherent sparsity-resolution trade-off when recognizing subtle micro-motions.

References

- [1] Tasweer Ahmad, Lianwen Jin, Xin Zhang, Songxuan Lai, Guozhi Tang, and Luojun Lin. 2021. Graph convolutional neural network for human action recognition: A comprehensive survey. *IEEE Transactions on Artificial Intelligence* 2, 2 (2021), 128–145.
- [2] Yuxin Chen, Ziqi Zhang, Chunfeng Yuan, Bing Li, Ying Deng, and Weiming Hu. 2021. Channel-wise topology refinement graph convolution for skeleton-based action recognition. In *Proceedings of the IEEE/CVF international conference on computer vision*. 13359–13368.
- [3] Ke Cheng, Yifan Zhang, Xiangyu He, Weihang Chen, Jian Cheng, and Hanqing Lu. 2020. Skeleton-based action recognition with shift graph convolutional network. In *Proceedings of the IEEE/CVF conference on computer vision and pattern recognition*. 183–192.
- [4] Hyung-gun Chi, Myoung Hoon Ha, Seunggeun Chi, Sang Wan Lee, Qixing Huang, and Karthik Ramani. 2022. Infogcn: Representation learning for human skeleton-based action recognition. In *Proceedings of the IEEE/CVF conference on computer vision and pattern recognition*. 20186–20196.
- [5] Shikuang Deng, Yuhang Li, Shanghang Zhang, and Shi Gu. 2022. Temporal efficient training of spiking neural network via gradient re-weighting. *arXiv preprint arXiv:2202.11946* (2022).
- [6] Jeonghyeok Do and Munchurl Kim. 2024. Skateformer: skeletal-temporal transformer for human action recognition. In *European Conference on Computer Vision*. Springer, 401–420.
- [7] Yong Du, Wei Wang, and Liang Wang. 2015. Hierarchical recurrent neural network for skeleton based action recognition. In *Proceedings of the IEEE conference on computer vision and pattern recognition*. 1110–1118.
- [8] Haodong Duan, Yue Zhao, Kai Chen, Dahua Lin, and Bo Dai. 2022. Revisiting skeleton-based action recognition. In *Proceedings of the IEEE/CVF conference on computer vision and pattern recognition*. 2969–2978.
- [9] Wei Fang, Zhaofei Yu, Yanqi Chen, Tiejun Huang, Timothée Masquelier, and Yonghong Tian. 2021. Incorporating learnable membrane time constant to enhance learning of spiking neural networks. In *Proceedings of the IEEE/CVF International Conference on Computer Vision*. 2661–2671.
- [10] Y. Fang, Z. Wang, L. Zhang, and et al. 2025. Spiking wavelet transformer. In *European Conference on Computer Vision*. Springer, 19–37.
- [11] Liqi Feng, Yaqin Zhao, Wenxuan Zhao, and Jiayi Tang. 2022. A comparative review of graph convolutional networks for human skeleton-based action recognition. *Artificial Intelligence Review* 55, 5 (2022), 4275–4305.
- [12] Samanwoy Ghosh-Dastidar and Hojjat Adeli. 2009. Spiking neural networks. *International journal of neural systems* 19, 04 (2009), 295–308.
- [13] Mark Horowitz. 2014. 1.1 computing’s energy problem (and what we can do about it). In *2014 IEEE international solid-state circuits conference digest of technical papers (ISSCC)*. IEEE, 10–14.
- [14] Ameer Hamza Khan, Xinwei Cao, Chunbo Luo, Shiqing Zhang, Wenping Guo, Vasilios N Katsikis, and Shuai Li. 2025. Spiking neural networks: a comprehensive survey of training methodologies, hardware implementations and applications. *Artificial Intelligence Science and Engineering* 1, 3 (2025), 175–207.
- [15] Petr Lansky, Pavel Sanda, and Jufang He. 2006. The parameters of the stochastic leaky integrate-and-fire neuronal model. *Journal of Computational Neuroscience* 21, 2 (2006), 211–223.
- [16] Donghyun Lee, Yuhang Li, Youngeun Kim, Shiting Xiao, and Priyadarshini Panda. 2025. Spiking transformer with spatial-temporal attention. In *Proceedings of the IEEE/CVF Conference on Computer Vision and Pattern Recognition*. 13948–13958.
- [17] Jungho Lee, Minhyeok Lee, Dogyoon Lee, and Sangyoun Lee. 2023. Hierarchically decomposed graph convolutional networks for skeleton-based action recognition. In *Proceedings of the IEEE/CVF international conference on computer vision*. 10444–10453.
- [18] Jun Liu, Amir Shahroudy, Mauricio Perez, Gang Wang, Ling-Yu Duan, and Alex C Kot. 2019. Ntu rgb+ d 120: A large-scale benchmark for 3d human activity understanding. *IEEE transactions on pattern analysis and machine intelligence* 42, 10 (2019), 2684–2701.
- [19] Jun Liu, Amir Shahroudy, Dong Xu, Alex C Kot, and Gang Wang. 2017. Skeleton-based action recognition using spatio-temporal LSTM network with trust gates. *IEEE transactions on pattern analysis and machine intelligence* 40, 12 (2017), 3007–3021.
- [20] Jun Liu, Gang Wang, Ling-Yu Duan, Kamila Abdiyeva, and Alex C Kot. 2017. Skeleton-based human action recognition with global context-aware attention LSTM networks. *IEEE Transactions on Image Processing* 27, 4 (2017), 1586–1599.
- [21] Yi Liu, Ruyi Liu, Yuzhi Hu, Mengyao Wu, Wentian Xin, Qiguang Miao, Shuai Wu, and Long Li. 2025. A Systematic Review of Skeleton-Based Action Recognition: Methods, Challenges, and Future Directions. *IEEE Transactions on Neural Networks and Learning Systems* (2025).
- [22] Z. Liu, H. Zhang, Z. Chen, and et al. 2020. Disentangling and unifying graph convolutions for skeleton-based action recognition. In *Proceedings of the IEEE/CVF conference on computer vision and pattern recognition*. 143–152.
- [23] Margaret Livingstone and David Hubel. 1988. Segregation of form, color, movement, and depth: anatomy, physiology, and perception. *Science* 240, 4853 (1988), 740–749.
- [24] William H Merigan and JH8460898 Maunsell. 1993. How parallel are the primate visual pathways? *Annual review of neuroscience* (1993).
- [25] Woomin Myung, Nan Su, Jing-Hao Xue, and Guijin Wang. 2024. Degcn: Deformable graph convolutional networks for skeleton-based action recognition. *IEEE Transactions on Image Processing* 33 (2024), 2477–2490.
- [26] Chiara Plizzari, Marco Cannici, and Matteo Matteucci. 2021. Skeleton-based action recognition via spatial and temporal transformer networks. *Computer Vision and Image Understanding* 208 (2021), 103219.
- [27] Hao hao Qu, Liangbo Ning, Rui An, Wenqi Fan, Tyler Derr, Hui Liu, Xin Xu, and Qing Li. 2024. A survey of mamba. *arXiv preprint arXiv:2408.01129* (2024).
- [28] Bin Ren, Mengyuan Liu, Runwei Ding, and Hong Liu. 2024. A survey on 3d skeleton-based action recognition using learning method. *Cyborg and Bionic Systems* 5 (2024), 0100.
- [29] Amir Shahroudy, Jun Liu, Tian-Tsong Ng, and Gang Wang. 2016. Ntu rgb+ d: A large scale dataset for 3d human activity analysis. In *Proceedings of the IEEE conference on computer vision and pattern recognition*. 1010–1019.
- [30] Lei Shi, Yifan Zhang, Jian Cheng, and Hanqing Lu. 2019. Two-stream adaptive graph convolutional networks for skeleton-based action recognition. In *Proceedings of the IEEE/CVF conference on computer vision and pattern recognition*. 12026–12035.
- [31] Shriyank Somvanshi, Md Monzurul Islam, Mahmuda Sultana Mimi, Sazzad Bin Bashar Polock, Gaurab Chhetri, and Subasish Das. 2025. From s4 to mamba: A comprehensive survey on structured state space models. *arXiv preprint arXiv:2503.18970* (2025).
- [32] J. Wang, X. Nie, and Y. Xia. 2014. Cross-view action modeling, learning and recognition. In *Proceedings of the IEEE conference on computer vision and pattern recognition*. 2649–2656.
- [33] Ziqing Wang, Yuetong Fang, Jiahang Cao, Qiang Zhang, Zhongrui Wang, and Renjing Xu. 2023. Masked spiking transformer. In *Proceedings of the IEEE/CVF international conference on computer vision*. 1761–1771.
- [34] Yujie Wu, Lei Deng, Guoqi Li, Jun Zhu, and Luping Shi. 2018. Spatio-temporal backpropagation for training high-performance spiking neural networks. *Frontiers in neuroscience* 12 (2018), 331.

- [35] Jianyang Xie, Yanda Meng, Yitian Zhao, Anh Nguyen, Xiaoyun Yang, and Yalin Zheng. 2024. Dynamic semantic-based spatial graph convolution network for skeleton-based human action recognition. In *Proceedings of the AAAI conference on artificial intelligence*, Vol. 38. 6225–6233.
- [36] Sijie Yan, Yuanjun Xiong, and Dahua Lin. 2018. Spatial temporal graph convolutional networks for skeleton-based action recognition. In *Proceedings of the AAAI conference on artificial intelligence*, Vol. 32.
- [37] Man Yao, Huajin Gao, Guangshe Zhao, Dingjian Wang, Yihan Lin, Zhaoxu Yang, and Guoqi Li. 2022. GLIF: A unified gated leaky integrate-and-fire neuron for spiking neural networks. In *Advances in Neural Information Processing Systems*, Vol. 35. 32160–32171.
- [38] M. Yao, J. Hu, T. Hu, and et al. 2024. Spike-driven transformer v2: Meta spiking neural network architecture inspiring the design of next-generation neuromorphic chips. *arXiv preprint arXiv:2404.03663* (2024).
- [39] Man Yao, Jiakui Hu, Zhaokun Zhou, Li Yuan, Yonghong Tian, Bo Xu, and Guoqi Li. 2023. Spike-driven transformer. *Advances in neural information processing systems* 36 (2023), 64043–64058.
- [40] Lixing Yu, Hanqi Chen, Ziming Wang, Shaojie Zhan, Jiankun Shao, Qingjie Liu, and Shu Xu. 2024. Spikingvit: A multiscale spiking vision transformer model for event-based object detection. *IEEE Transactions on Cognitive and Developmental Systems* 17, 1 (2024), 130–146.
- [41] Jiaxu Zhang, Yifan Jia, Wei Xie, and Zhigang Tu. 2022. Zoom transformer for skeleton-based group activity recognition. *IEEE Transactions on Circuits and Systems for Video Technology* 32, 12 (2022), 8646–8659.
- [42] Pengfei Zhang, Cuiling Lan, Junliang Xing, Wenjun Zeng, Jianru Xue, and Nanning Zheng. 2019. View adaptive neural networks for high performance skeleton-based human action recognition. *IEEE transactions on pattern analysis and machine intelligence* 41, 8 (2019), 1963–1978.
- [43] Pengfei Zhang, Cuiling Lan, Wenjun Zeng, Junliang Xing, Jianru Xue, and Nanning Zheng. 2020. Semantics-guided neural networks for efficient skeleton-based human action recognition. In *proceedings of the IEEE/CVF conference on computer vision and pattern recognition*. 1112–1121.
- [44] Naichuan Zheng, Yuchen Du, Hailun Xia, and Zeyu Liang. 2025. Signal-SGN: A Spiking Graph Convolutional Network for Skeleton Action Recognition via Learning Temporal-Frequency Dynamics. In *Proceedings of the 33rd ACM International Conference on Multimedia*. 1539–1548.
- [45] Naichuan Zheng, Hailun Xia, Zeyu Liang, and Yuchen Du. 2025. MK-SGN: A spiking graph convolutional network with multimodal fusion and knowledge distillation for skeleton-based action recognition. *Neurocomputing* (2025), 131796.
- [46] Yuxuan Zhou, Zhi-Qi Cheng, Chao Li, Yanwen Fang, Yifeng Geng, Xuansong Xie, and Margret Keuper. 2022. Hypergraph transformer for skeleton-based action recognition. *arXiv preprint arXiv:2211.09590* (2022).
- [47] Zhaokun Zhou, Yuesheng Zhu, Chao He, Yaowei Wang, Shuicheng Yan, Yonghong Tian, and Li Yuan. 2022. Spikformer: When spiking neural network meets transformer. *arXiv preprint arXiv:2209.15425* (2022).

In this supplementary material, we provide comprehensive additional details and analyses that were omitted from the main manuscript due to space constraints. Specifically, Appendix A elaborates on the specifics of the three large-scale skeleton datasets and their corresponding evaluation protocols. Following this, Appendix B outlines the detailed hyperparameter settings and training configurations to ensure the full reproducibility of our experiments. Moreover, Appendix D presents a rigorous theoretical analysis of the energy efficiency and Synaptic Operations (SOPs) of our S3T-Former, quantitatively proving its ultra-low power consumption. Finally, Appendix E offers extended qualitative visualizations, including additional topological routing maps, to further elucidate the internal reasoning mechanisms of our model.

A Datasets and Evaluation Protocols

NTU RGB+D 60 [29] is a widely used large-scale benchmark for skeleton-based action recognition, comprising 56,880 video samples across 60 action classes. The actions are performed by 40 distinct subjects and captured simultaneously by three Microsoft Kinect v2 cameras from different viewing angles. Following the authoritative guidelines, we adopt two standard evaluation protocols: **Cross-Subject (X-Sub)**, where the 40 subjects are equally split into training and testing groups, and **Cross-View (X-View)**, where sequences captured by cameras 2 and 3 are utilized for training, while those from camera 1 are reserved for testing.

NTU RGB+D 120 [18] is the comprehensive extension of NTU RGB+D 60, currently serving as the most challenging and largest dataset in this domain. It encompasses 114,480 skeletal sequences spanning 120 action classes, performed by 106 subjects across 32 distinct camera setups. We strictly adhere to the official evaluation protocols: **Cross-Subject (X-Sub)**, which divides the 106 subjects into 53 training and 53 testing groups, and **Cross-Setup (X-Set)**, where the 32 camera setups are partitioned into even IDs for training and odd IDs for testing.

Northwestern-UCLA (NW-UCLA) [32] contains 1,494 video sequences representing 10 daily action categories. These actions are performed by 10 different subjects and captured by three Kinect cameras from varying viewpoints. Following the standard Cross-View evaluation protocol, we use samples from the first two cameras (V1 and V2) for training, and evaluate the model’s performance on the samples from the third camera (V3).

B Implementation Details and Hyperparameters

B.1 Implementation Details

Our proposed S3T-Former is implemented using the PyTorch framework in conjunction with the open-source SpikingJelly library. To ensure full reproducibility, we detail the implementation configurations across three primary dimensions: network instantiation, data processing, and optimization strategy.

Network Configurations and Spiking Dynamics. The core backbone is constructed by stacking $L = 6$ S3T Blocks, with the spatial topology routing decoupled into $H = 8$ independent attention heads. The embedding dimension D and the simulation time step T are dynamically scaled to instantiate different model variants (e.g., $D \in \{256, 384\}$ and $T \in \{8, 16, 32\}$) for comprehensive comparisons.

For the neuromorphic dynamics, we employ LIF neurons with a fixed firing threshold of $U_{th} = 0.5$ and a membrane leakage factor of $\tau = 0.5$. Since the binary spike generation (Heaviside step function) is inherently non-differentiable, we utilize the Arctangent (ATan) surrogate gradient function with a shape parameter of $\alpha = 2.0$ to enable stable backpropagation through time (BPTT).

Data Preprocessing and Augmentation. To strictly align the raw skeleton data with the SNN simulation time windows, each action sequence is uniformly sampled or padded to a fixed temporal length T . The 3D spatial coordinates are zero-centered based on the root joint (the “spine” node) to ensure translation invariance. Notably, we strictly refrain from employing any spatial or temporal skeleton data augmentation techniques (such as random rotation, scaling, or shear) during training. This deliberate constraint is designed to rigorously validate the inherent representational robustness and kinematic reasoning capabilities of our pure-spiking design, free from the performance inflation typically induced by heavy augmentations.

Optimization and Temporal Efficient Training. The network is trained from scratch for 250 epochs using a total batch size of 64. We optimize the model using the AdamW optimizer with a base learning rate of 0.01 and a weight decay of 0.0005. To stabilize the initial learning phase, we apply a 10-epoch linear warmup, followed by a cosine annealing learning rate schedule that gradually decays to 1×10^{-5} . To effectively optimize the deep temporal dynamics without suffering from gradient vanishing, we apply the Temporal Efficient Training (TET) loss directly on the continuous outputs of our U-Readout integrator. Specifically, the cross-entropy loss is computed and averaged across all temporal simulation steps to provide dense objective supervision. All experiments are accelerated using Automatic Mixed Precision (AMP) to reduce memory footprint, seamlessly distributed across four NVIDIA Tesla V100 GPUs.

C PyTorch-like Pseudocode of S3T-Former

To facilitate future research and ensure strict reproducibility, we provide the PyTorch-style pseudocode for the core S3T-Attn in Listing 1. The code explicitly demonstrates that our architecture strictly operates on discrete binary spikes. Specifically, the local binding is executed via negligible bitwise AND operations (“*”), the spatial routing utilizes parameter-free conditional additions (“einsum” with binary operands), and the temporal integration is achieved through a linear-time $O(T)$ state-space loop. This implementation completely circumvents the dense $O(N^2 \times D)$ floating-point attention matrices typical of vanilla Transformers.

```
import torch
from torch import einsum

def s3t_attention(x, base_topo, learned_topo, alpha=0.8):
    # x: [T, B, C, N] (Time, Batch, Channels, Nodes)
    T, B, C, N = x.shape

    # 1. ATG-QKV Generation
    x_grad = torch.cat([torch.zeros_like(x[0:1]),
                        torch.abs(x[1:]-x[:-1])])
    qkv_in = alpha * x_grad + (1 - alpha) * x # Soft-ATG blending
```

```

q = LIF_Q(Linear_Q(qkv_in)) # Binary motion
  queries {0, 1}
k = LIF_K(Linear_K(qkv_in)) # Binary motion
  keys {0, 1}
v = LIF_V(Linear_V(x))      # Binary static
  values {0, 1}

# 2. Local Binding (Zero MACs, pure bitwise AND)
kv_local = k * v

# 3. Lateral Spiking Topology Routing (LSTR)
topo = torch.softmax(base_topo + learned_topo,
  dim=-1)
# Conditional additions via binary operands
kv_spatial = einsum('h i j, t b h j d -> t b h
  i d', topo, kv_local)
kv_spike = LIF_Buffer(kv_spatial)

# 4. Spiking State-Space (S3) Engine
decay = torch.clamp(torch.sigmoid(decay_w),
  0.01, 0.99)
M = torch.zeros_like(kv_spike[0])
out = torch.empty_like(q)

for t in range(T):
  M = decay * M + (1 - decay) * kv_spike[t] #
    Temporal accumulation
  out[t] = q[t] * M                          #
    Spike-gated retrieval

# 5. Output Projection
return LIF_Out(Linear_Out(out)) + x

```

Listing 1: PyTorch-like Pseudocode of S3T-Former Attention.

D Hardware-Aware Energy and Spiking Sparsity Analysis

To quantitatively validate the low-power characteristics of the proposed S3T-Former, we conduct a hardware-aware energy consumption analysis based on the standard 45nm CMOS technology [13]. In standard Artificial Neural Networks (ANNs), the primary computational cost stems from dense floating-point Multiply-Accumulate (MAC) operations. The theoretical energy consumption for an ANN is directly proportional to its total FLOPs ($E_{\text{ANN}} = O_{\text{FLOPs}} \times E_{\text{MAC}}$), where $E_{\text{MAC}} = 4.6$ pJ represents the energy cost of a 32-bit MAC operation.

For our S3T-Former, the computational graph is fundamentally hybrid. Based on the discrete or continuous nature of the input tensors, the overall operations are strictly decoupled into floating-point MACs and spike-driven Synaptic Operations (SOPs). Furthermore, during inference, all Batch Normalization (BN) operations are analytically folded into their preceding linear layers, incurring zero additional computational energy.

1. Floating-Point MAC Operations: MAC operations exclusively occur when processing continuous values, including the representation extraction in M-ASE, temporal integration within the S3-Engine, and the classification head. The total MAC operations are the sum of their respective FLOPs:

$$O_{\text{MAC}} = O_{\text{ASE}} + \sum_{l=1}^L (O_{\text{S3-Engine}}^{(l)} + O_{\text{proj}}^{(l)}) + O_{\text{FC_head}}. \quad (12)$$

2. Spike-Driven Synaptic Operations (SOPs): The core efficiency originates from the spike-driven modules, including the ATG-QKV generation, the Lateral Spiking Topology Routing (LSTR), and the Spiking FFN (MLP). Because the inputs to these layers are binary spikes $S \in \{0, 1\}$, dense matrix multiplications mathematically degenerate into sparse Accumulate (AC) operations ($E_{\text{AC}} = 0.9$ pJ). The total number of SOPs is intrinsically tied to the empirical spike firing rate (Fr):

$$O_{\text{SOP}} = \sum_{l=1}^L \sum_{m \in \mathcal{M}_{\text{spike}}} O_m^{(l)} \times Fr_m^{(l)}, \quad (13)$$

where $\mathcal{M}_{\text{spike}} = \{Q, K, V, \text{LSTR}, \text{MLP1}, \text{MLP2}\}$. Notably, local binding ($K \odot V$) reduces to bitwise AND operations, the energy cost of which is negligible compared to ACs.

Empirical Sparsity and Energy Estimation: To empirically substantiate the SOP reduction, we systematically profile the layer-wise spike firing rates (Fr) of our standard S3T-Former ($T = 16$). As reported in Table 5, thanks to the dynamic filtering of the LSTR module and the event-driven nature of our architecture, the firing rates of the critical bottlenecks plummet as the network deepens. For instance, the Topo Buffer firing rate drops from 10.09% in Block 1 to a mere 1.91% in Block 6. Similarly, the MLP 1 layer—which scales the channel dimension by 4× and encompasses the majority of the network’s parameters—maintains an extreme sparsity ranging from 4.20% down to 1.38%.

Given that an AC operation consumes roughly 5× less energy than a MAC operation, the theoretical energy for the spike-driven modules is strictly bounded by $\sim \frac{1}{5} \times Fr$. With our global average firing rate at $\sim 16.9\%$ and the most parameter-heavy expansion layers operating at $< 3\%$ sparsity, the SOP energy is drastically minimized. Even when accounting for the continuous MAC operations in the M-ASE and S3-Engine, the total theoretical energy consumption ($E_{\text{SNN}} = O_{\text{MAC}} \times E_{\text{MAC}} + O_{\text{SOP}} \times E_{\text{AC}}$) is conservatively estimated to be strictly within **10%** of a structurally equivalent dense ANN. This rigorously confirms the absolute power superiority of our neuromorphic design without compromising recognition accuracy.

E Extended Qualitative Results

E.1 Full Confusion Matrix and Failure Diagnosis

For absolute transparency and to provide deeper insights into the boundary conditions of our neuromorphic design, we present the full confusion matrix for the NTU RGB+D 60 evaluation in Fig. 9.

While S3T-Former achieves a strong overall accuracy of 84.94%, a diagnostic inspection of the confusion matrix reveals a highly specific and consistent failure mode. The red dashed lines in Fig. 9 highlight the top three most challenging categories: Class 11 (Error Rate: 47.79%), Class 28 (Error Rate: 43.64%), and Class 10 (Error Rate: 41.76%). In the NTU RGB+D 60 dataset, these classes correspond to "Writing," "Playing with phone/tablet," and "Reading," respectively.

These actions share a fundamental biomechanical similarity: they involve seated postures with extremely fine-grained, localized micro-motions of the fingers and wrists, accompanied by minimal macro-skeletal displacement. Because our Asymmetric Temporal-Gradient QKV (ATG-QKV) mechanism is explicitly engineered to

Table 5: Layer-wise average spike firing rates (Fr , %) of the standard S3T-Former ($T = 16$). MLP 1 and MLP 2 denote the channel expansion ($4\times$) and projection layers within the Spiking FFN, respectively. The most parameter-heavy expansion modules (Topo Buffer and MLP 1) exhibit extreme deep-layer sparsity.

Block	ATG-QKV Generation			Spatial-Temporal Routing(LSTR+S3)		Spiking FFN (MLP)	
	Q	K	V	Topo Buffer	Attn Out	MLP 1 (Exp.)	MLP 2 (Proj.)
1	27.49	53.00	44.24	10.09	28.15	4.20	20.60
2	21.43	49.31	27.71	2.95	23.17	2.45	17.62
3	24.77	56.07	24.19	1.86	25.90	1.90	20.53
4	24.26	53.65	22.42	1.32	22.93	1.56	28.19
5	19.77	55.84	19.13	1.31	30.01	1.38	34.24
6	16.30	67.10	19.65	1.91	41.76	1.54	45.23
Avg.	22.33	55.82	26.22	3.24	28.65	2.17	27.73

aggressively filter out static spatial features and fire exclusively on physical motion gradients to maximize energy efficiency, it generates an exceptionally sparse event stream for these specific actions. Consequently, the network inadvertently sacrifices the high-resolution static spatial cues necessary to robustly distinguish between identical hand-to-chest proximities (e.g., holding a book versus holding a phone).

This diagnostic reveals an inherent trade-off in current pure-spiking architectures between extreme temporal sparsity and micro-motion spatial resolution. Addressing this bottleneck—potentially through multi-scale dynamic thresholds or localized firing amplification—remains an exciting avenue for advancing neuromorphic action recognition.

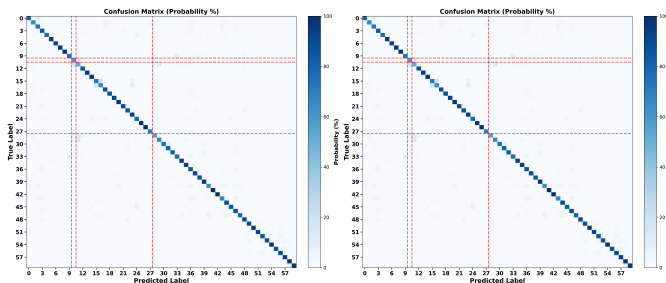


Figure 9: Full confusion matrix of S3T-Former on the NTU RGB+D 60 benchmark. The red dashed lines explicitly highlight the top three most confusing action classes: Class 10 (Reading), Class 11 (Writing), and Class 28 (Playing with phone/tablet). These failures highlight the inherent difficulty of distinguishing highly localized micro-motions within an aggressively sparse, event-driven SNN framework.

E.2 Layer-wise Skeleton Spiking Heatmaps: The Semantic Sparsity Funnel

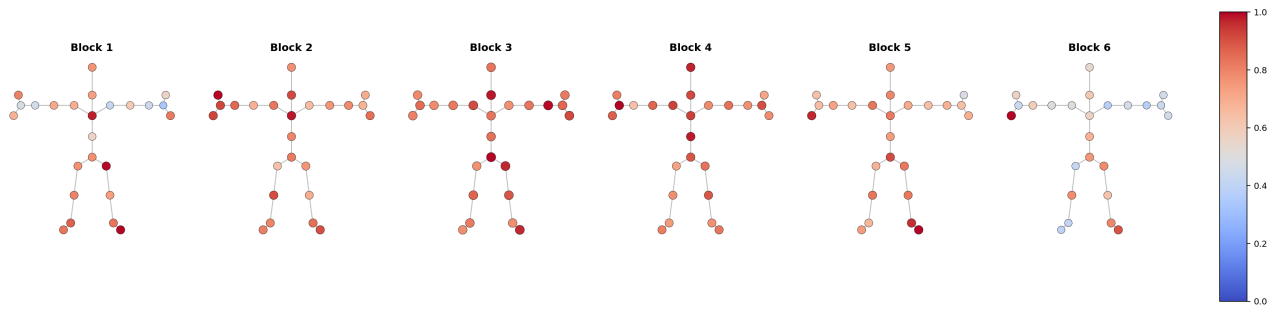
To intuitively visualize the extreme spatial sparsity and the layer-wise representational shift achieved by our architecture, we project the accumulated query (Q) spike firing rates directly onto the 3D human skeleton. In Fig. 10, we present the layer-wise evolution (from

Block 1 to Block 6) across five distinct action categories: Throwing (Class 6), Kicking (Class 23), Jumping Up (Class 26), Falling (Class 42), and Punch/Slap (Class 49).

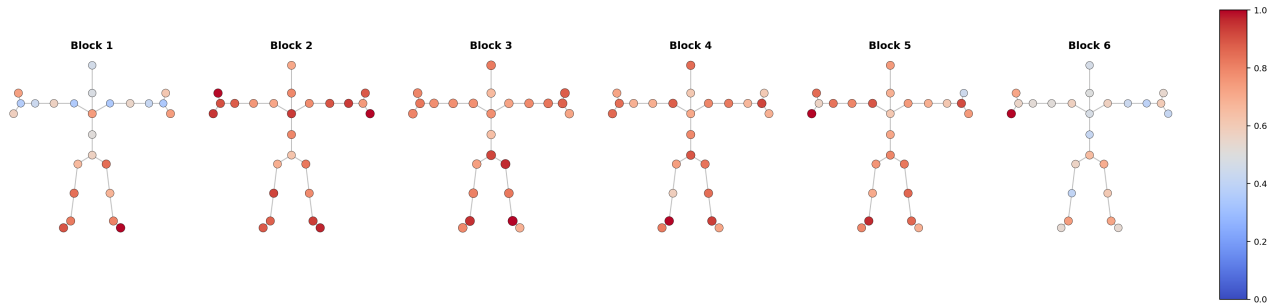
The visualizations reveal a profound "sparsity funnel" effect, demonstrating that our S3T-Former does not merely perform "on-demand energy allocation," but effectively acts as a powerful **Spatio-Temporal Semantic Hard-Attention** mechanism. The progression follows three distinct representational phases:

- **Kinematic Tracking Phase (Blocks 1-2):** In the shallow layers, the network faithfully tracks the raw physical kinetic chain. For instance, in the "Kicking" (Class 23) and "Throwing" (Class 6) actions, the entire active limb (leg or arm) alongside the stabilizing torso exhibits high firing rates (red). The network allocates energy to capture the low-level physical deformations across multiple related joints.
- **Spatial Pruning Phase (Blocks 3-4):** As representations propagate deeper, the Lateral Spiking Topology Routing (LSTR) actively filters out redundant spatial noise. Peripheral joints that only serve as physical connectors begin to go dormant (turning light blue), while the core action centers remain highly active.
- **Semantic Focus Phase (Blocks 5-6):** In the deepest layers, the network achieves extreme sparsity. The physical skeleton becomes largely dormant, and the remaining spikes are exclusively clustered at the most discriminative topological endpoints defining the action's semantic core. For striking actions like "Punching" (Class 49) and "Kicking" (Class 23), the energy is sharply focused on the extreme end-effectors (the fist and the ankle). Fascinatingly, for global body momentum actions like "Falling" (Class 42) and "Jumping" (Class 26), the deep layers shift their focus toward the spine and the center of gravity.

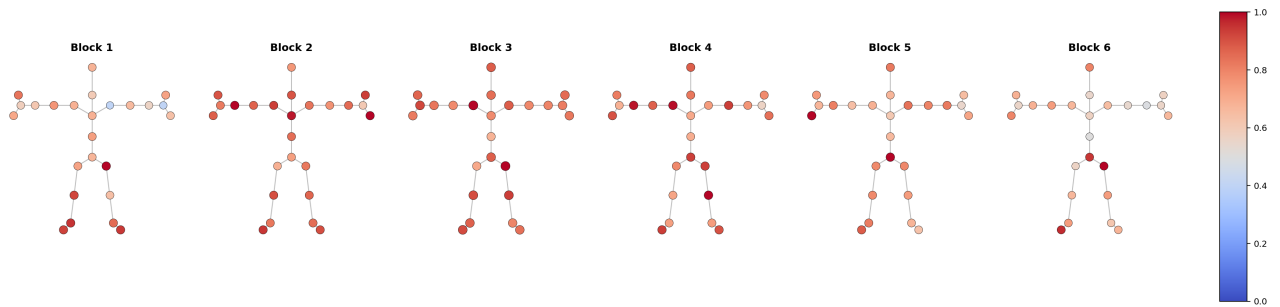
This visual evidence mathematically and biologically validates our design: as the feature dimensions expand in deeper stages, the network systematically zeroes out irrelevant physical tracking, condensing the complex input into ultra-sparse, highly discriminative semantic signatures. This guarantees our minimal energy footprint while simultaneously boosting recognition accuracy.



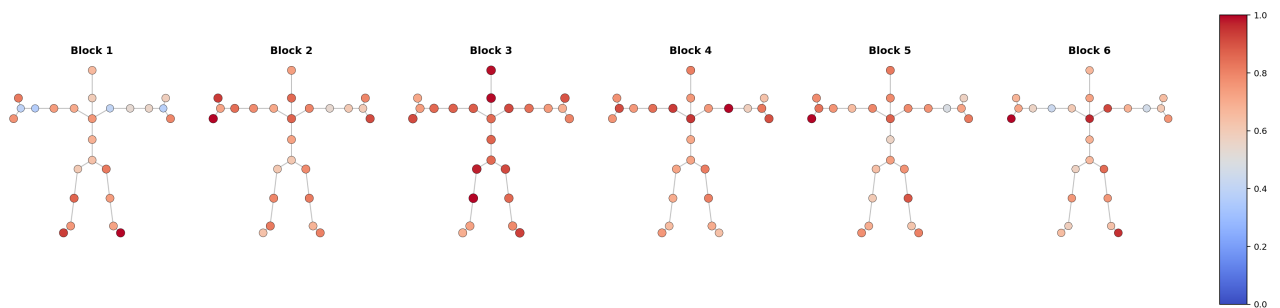
(a) Class 6: Throwing



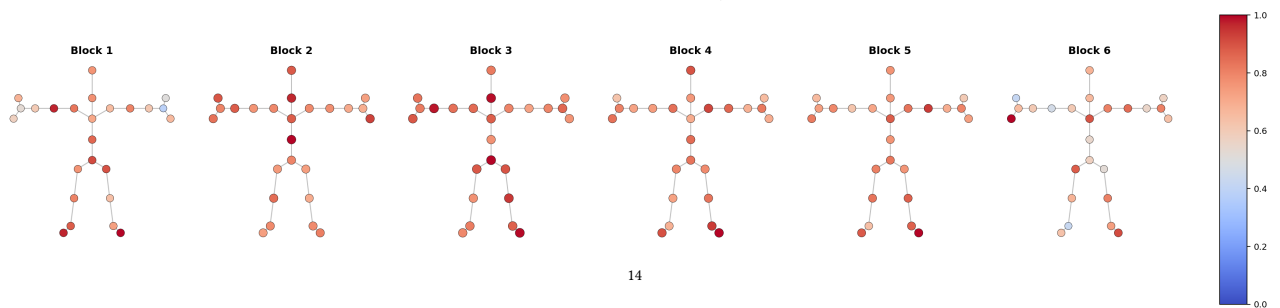
(b) Class 23: Kicking something



(c) Class 26: Jump up



(d) Class 42: Falling



(e) Class 49: Punch/Slap other person

Figure 10: Layer-wise evolution of spiking heatmaps. Red indicates active firing, while blue denotes zero-energy dormancy. This illustrates how the network funnels dense low-level kinematics into ultra-sparse semantic endpoints at deeper layers.